Geophysical Research Letters, 48, e2021GL095213, 2021, doi:10.1029/2021GL095213

Coseismic and early postseismic deformation due to the 2021 M7.4 Maduo (China) earthquake

Zeyu Jin[1], **Yuri Fialko**[1]

[1]Institute of Geophysics and Planetary Physics, Scripps Institution of Oceanography, University of California San Diego, La Jolla, CA 92093, USA.

Key Points:

- We use Sentinel-1 Synthetic Aperture Radar (SAR) data to derive a finite fault model for the 2021 M7.4 Maduo (Qinghai, China) earthquake
- The along-strike averaged coseismic slip has a maximum at depth of 3-4 km, with an amplitude of ∼2.5 m.
- Up to ∼0.1 m of afterslip occurred on the fault trace in the first month following the earthquake.

Corresponding author: Yuri Fialko, yfialko@ucsd.edu

Abstract

The 2021 Maduo earthquake ruptured a 150 km-long left-lateral fault in the north-east Tibet. We used Synthetic Aperture Radar data collected by the Sentinel-1A/B satellites within days of the earthquake to derive a finite fault model and investigate the details of slip distribution with depth. We generated coseismic interferograms and pixel offsets from different look directions corresponding to the ascending and descending satellite orbits. At the eastern end the rupture bifurcated into two sub-parallel strands, with larger slip on the northern strand. Inversions of coseismic displacements show maximum slip to the east of the epicenter. The averaged coseismic slip has a peak at depth of 3-4 km, similar to slip distributions of a number of shallow strike-slip earthquakes. Postseismic observations over several weeks following the Maduo earthquake reveal surface slip with amplitude up to 0.1 m that at least partially eliminated the coseismic slip deficit in the uppermost crust.

Plain language summary

A large earthquake occurred in a remote area of north-east Tibet (Qinghai Province, China) on May 21, 2021. The earthquake produced a 150 km-long rupture with surface offsets up to several meters. We used data collected by orbiting satellites to map motions of the Earth's surface that occurred during and shortly after the earthquake. The measured surface displacements were used to constrain the rupture geometry and slip distribution at depth. Best-fitting models suggest that rupture occurred on a sub-vertical fault steeply dipping to the north, with most of slip occurring to the east of the earthquake epicenter. The maximum coseismic slip occurred in the uppermost crust, in the depth interval of 3-4 km below the Earth's surface. A decrease in the fault offsets toward the Earth's surface is likely caused by an increased frictional resistance of the shallow layer to rapid coseismic slip. Satellite observations made in the first month after the earthquake reveal that the shallow part of the fault is slowly catching up with a deeper part to make up for the difference in the amount of slip produced during the earthquake.

1 Introduction

The 2021 Maduo earthquake occurred at 18:04 on May 21 (GMT) in the north-eastern part of the Tibetan Plateau (Qinghai Province, China), to the southeast of the Eling Lake (Figure 1). The focal mechanism and the distribution of aftershocks indicate that the earthquake ruptured a $\sim$ 150 km long left-lateral strike-slip fault (Figure 1). The earthquake rupture is located between the Kunlun and Xiangshuihe faults, two major left-lateral faults accommodating the eastward extrusion of Tibet (e.g., Tapponnier et al., 1982; Thatcher, 2007; Searle et al., 2011). The fault that produced the 2021 Maduo earthquake partially overlaps with a previously recognized unnamed left-lateral fault (HimaTibetMap database, Taylor & Yin, 2009); the two faults are of comparable length, but the 2021 rupture on average has a more easterly trend. The moment magnitude of the Maduo earthquake determined from seismic data varies from 7.3 (W-phase moment tensor magnitude, USGS, 2021a) to 7.5 (centroid moment tensor magnitude, USGS, 2021b).

The area adjacent to the 2021 rupture has been very active seismically, with a number of strong (M>6) events that occurred over the last century (Figure 1). The largest of these events was the 1937 M7.5 Tuosuo Lake earthquake that ruptured the eastern end of the Kunlun fault (Guo et al., 2007). The USGS estimate of the moment magnitude of the 1937 event is 7.8 (USGS, 2021c). The Kunlun fault system recently produced several other major earthquakes, including the 1997 M7.6 Manyi (Funning et al., 2007) and the 2001 M7.8 Kokoxilli (Klinger et al., 2005) earthquakes that occurred further to the west.

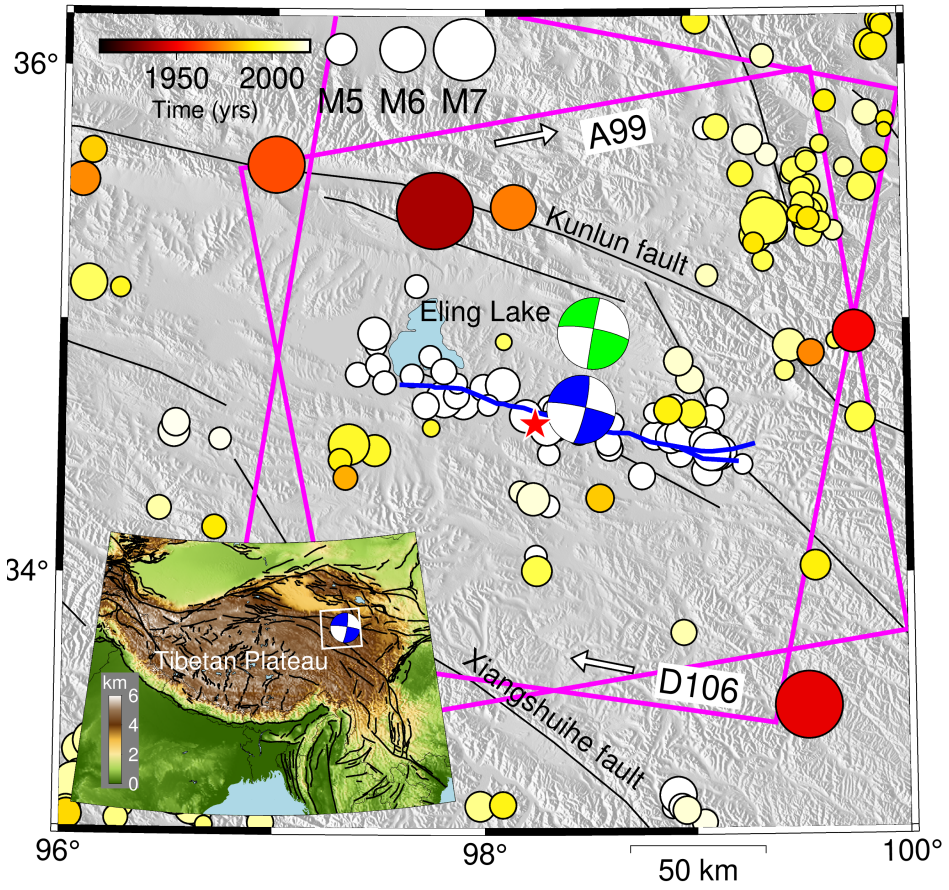

Figure 1. Tectonic setting of the 2021 M7.4 Maduo earthquake. Blue curvy line denotes the rupture trace mapped using the Sentinel-1 range offsets (Figure S3). Red star denotes the epicenter. White-and-blue "beach ball" denotes the centroid location and the focal mechanism from the Global CMT catalog (Ekström et al., 2012). White-and-green "beach ball" denotes the focal mechanism corresponding to our finite fault model. Thin black lines denote active faults (Taylor & Yin, 2009). Color circles denote shallow (hypocenter depth less than 50 km) historic earthquakes up to July of 2021; color represents time, and size represents magnitude. Magenta rectangles denote swaths of Sentinel-1 SAR data used in this study. Arrows indicate the radar look direction. (Inset) Topography and fault map of the India-Eurasia collision zone.

In this paper we use Synthetic Aperture Radar (SAR) data collected by the Sentinel-1A and 1B satellites of the European Space Agency to investigate coseismic and early postseismic surface deformation due to the 2021 Maduo earthquake, map the rupture trace, and derive a fault slip model. We then discuss implications of space geodetic observations and inverse modeling for the mechanical properties of the upper crust in the study area and the problem of shallow slip deficit (Fialko et al., 2005; Kaneko & Fialko, 2011).

2 Data and methods

Sentinel-1 SAR data that most tightly bracket the origin time of the Maduo earthquake were acquired on May 20 and 26, 2021 from the ascending track 99, and the descending track 106 (see Tables S1 and S2 in the Supporting Information). All data were acquired in the Terrain Observation by Progressive Scan (TOPS) mode in C-band (radar wavelength of 56 mm). Each TOPS image consists of 3 subwaths, with a total swath width of $\sim$ 250 km, providing a complete coverage of the earthquake rupture from two distinct look directions corresponding to the ascending and descending satellite orbits (see Figure 1, and Figures S1 and S2 in Supporting Information).

We formed interferometric pairs using images taken before and after the earthquake (see tables S1 and S2 in Supporting Information) using GMTSAR (Sandwell et al., 2011). The topography contribution to the radar phase was calculated and removed using digital elevation data from the Shuttle Radar Topography Mission (SRTM) with 30 m resolution (Farr & Kobrick, 2000). Phase ambiguities due to possible changes in topography over a time period of 20 years since the acquisition of the SRTM data (e.g., Lin et al., 2006) are assumed to be negligible given relatively small perpendicular baselines of Sentinel-1 interferograms (Table S2). Phase delays due to propagation through the atmosphere are expected to be small compared to the meter-scale coseismic signals (e.g., Tymofyeyeva & Fialko, 2015) and are also neglected. The SAR images were co-registered using the Bivariate Enhanced Spectral Diversity (BESD) method (Wang et al., 2017). The method uses a double-differenced phase in the overlaps between the adjacent radar bursts to precisely co-register the focused radar images with the range- and azimuth-dependent alignment. The latter mitigates the impact of coseismic displacements that are large enough to cause phase discontinuities across the burst boundaries when images are aligned using a constant shift in the azimuth direction.

In the near field of the earthquake rupture, high gradients in surface displacements and/or intense damage result in decorrelation of the radar phase (see Figures S1 and S2). To avoid artifacts due to unwrapping errors in areas of low correlation, we unwrapped the radar phase using a conservative branch-cut algorithm (Goldstein et al., 1988). Each sub-swath was unwrapped separately, and the 2π phase ambiguities were resolved to ensure the phase continuity between the adjacent sub-swaths. To obtain surface displacements in the near field of the earthquake rupture where the radar phase cannot be confidently unwrapped, we computed pixel offsets in the range direction (Figure S3). The range offsets are equivalent to the interferometrically measured line of sight (LOS) displacements. The offsets are computed by cross-correlating the radar amplitude images taken before and after the earthquake. They are less precise than the differential phase measurements, but are not limited by the requirement of phase coherence. The range offsets complement the interferometry data by providing continuous measurements of surface displacements all the way to the rupture trace (Figures S1, S2 and S3). Because the amplitude of the near-field coseismic displacements is of the same order as the pixel size in radar range ($\sim$4 m), the signal-to-noise ratio (SNR) is quite high (Figure S3). We don't use the azimuth offsets because of a much larger pixel size in the azimuth direction, and the correspondingly lower SNR.

The computed range offsets reveal a displacement discontinuity that can be used to locate the rupture trace (Figure S3). Offsets from diverse projections are particularly helpful for identifying the surface rupture when the latter is not highly localized. The digitized rupture trace is shown as a blue wavy line in Figure 1 (also, see black lines in Figures S3a and S3b).

To invert the observed coseismic displacements for a slip distribution on the earthquake rupture, we sub-sampled the unwrapped interferograms and range offsets using a quad-tree algorithm (Jonsson et al., 2002; Simons et al., 2002). To avoid over-sampling in areas affected by high-frequency noise (atmospheric contributions, unwrapping errors, phase decorrelation, etc.), we sub-sampled the data iteratively using model predictions (Wang & Fialko, 2015). Following an initial inversion in which the best-fit slip model was obtained, the location of the data samples was determined by executing the gradient-based quad-tree algorithm on a model prediction. The obtained discretization cells were populated by the mean values of data from the original interferograms and offset maps. Usually, two or three iterations are sufficient to achieve a convergent set of data points. In order to capture the details of slip distribution near the Earth's surface, we more densely sampled the range offsets around the fault trace. Given a patch size of ~ 1 km at the shallowest part of the slip model, we sampled the near-field data starting at minimum spacing of ~ 250 m. The (spatially variable) unit look vectors for all data samples were computed by averaging the original values in the same cells as used for sub-sampling the displacement data.

The fault geometry at depth is not known a priori, and is usually either (i) assumed, (ii) constrained based on independent data such as precisely located aftershocks (e.g., Jin & Fialko, 2020), or (iii) inferred through non-linear inversions of surface displacement data (e.g., Fialko et al., 2005; Wang & Fialko, 2015; Dutta et al., 2021). We performed several inversions allowing for both vertical and non-vertical earthquake rupture. The rupture trace was approximated using several piece-wise linear segments that define planar rectangular sub-faults. Sub-faults were extended down-dip by 25 km, and sub-divided into slip patches which sizes gradually increase from about 1 km (along-strike and down-dip) at the top of the fault model to about 5-10 km at the bottom, following a geometric progression to ensure a nearly diagonal structure of the model resolution matrix (Fialko, 2004b). We computed Green's functions for the strike and dip components of slip on each patch for every observation point. As there are many more data points than the degrees of freedom, the system is over-determined and is solved by minimizing the L_2 norm of the residual. We applied a positivity constraint on strike-slip components, such that no slip was allowed to be right-lateral. No positivity constraints were imposed on the dip-slip components, but the latter were more strongly smoothed compared to the strike-slip components to avoid spatially oscillating slip patterns. The first-order Tikhonov regularization (e.g., Golub et al., 1999) was applied to avoid extreme variations in slip between the adjacent fault patches. At complex junctions involving more than 2 sub-faults (e.g., at the Y-shaped intersection at the eastern end of the earthquake rupture) we applied regularizing constraints that preserve the slip budget between the "parent" and the bifurcated strands, $U_p^j = U_{b1}^j + U_{b2}^j$, where U_p^j is the jth component of slip on a patch that belongs to the parent strand, and U_{b1}^j and U_{b2}^j are the respective components of slip on the adjacent slip patches that belong to the bifurcated branches $b1$ and $b2$. The adjacent fault patches of different strands were identified automatically based on proximity between the patch edges.

We further regularized the problem by imposing soft zero-slip boundary conditions (wU^j=0, where U^j is the jth component of an unknown slip vector, and w is a prescribed weight) at the fault edges, except at the top edge that was left unconstrained. The optimal values of the smoothness parameters were determined using the Chi-Squared statistics (e.g., Wang & Fialko, 2014; Jin & Fialko, 2020).

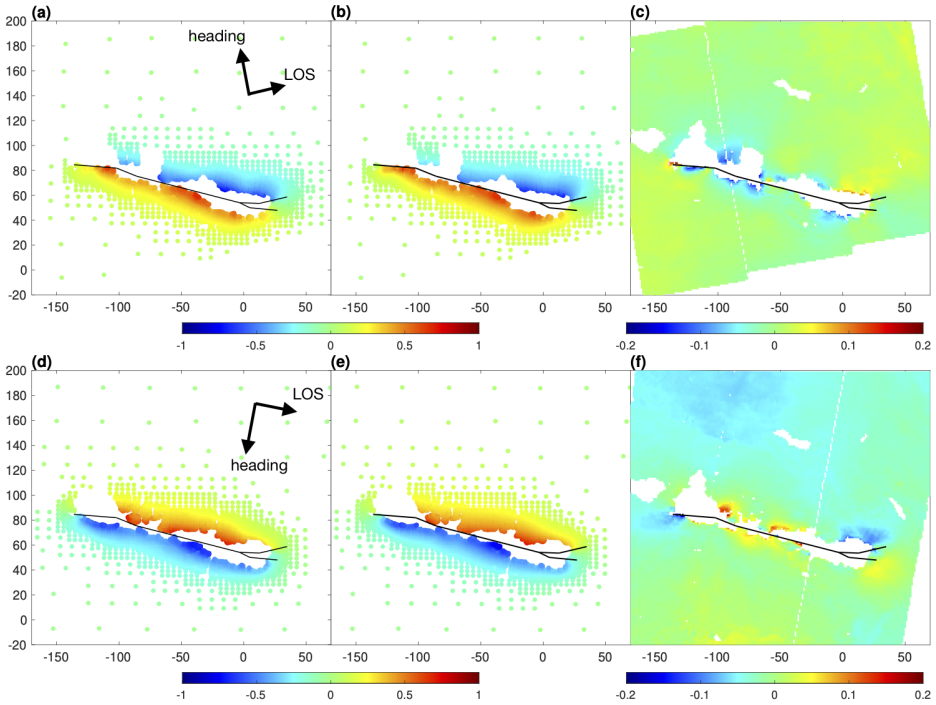

Figure 2. Sub-sampled coseismic LOS displacements (a,d), best-fit model predictions (b, e), and residuals (c, f) from the ascending (a-c) and descending (d-f) Sentinel-1 tracks (see Figures 1, S1, and S2). Black lines denote the modeled fault trace. Coordinate axes are in kilometers, with an origin at 99°E, 34°N. Arrows indicate the satellite heading and line of sight. Increases in radar range are deemed positive. Color scales are in meters.

We performed two sets of inversions, one using Green's functions for a homogeneous elastic halfspace (Okada, 1985), and another for a layered elastic halfspace (Wang et al., 2003). For the latter, we used elastic moduli from a one-dimensional (1-D) regional seismic velocity model of the north-eastern Tibet (Figure S4). Inversions taking into account a 3-D distribution of elastic moduli (e.g., Barbot, Fialko, & Sandwell, 2009) are not warranted given a lack of high-resolution seismic tomography models in the study area. We adopted the same fault geometry for the homogeneous and layered halfspace models. In case of layered models, rectangular fault patches were approximated by a superposition of point sources.

In each case (homogeneous and layered halfspace models) we performed a series of inversions in which we varied the fault dip angle $\pm 30°$ from the vertical, in 5° increments. For simplicity, all fault segments were assigned the same dip angle. The best fit is achieved for a fault that is steeply dipping to the north at 80-85 degrees (Figure S5).

Figure 2 shows the sub-sampled data points, predictions of the best-fit layered models, and residuals (the difference between the data and the model predictions) for the Sentinel-1 interferograms from the ascending and descending tracks. We compute residuals at the original (unsampled) resolution to illustrate the model fit to all of the data points, including those that were not used in the inversion. Figure S6 shows the model fit to the range offsets that constrain the shallow part of the slip model. Overall, the model fits the main features of the displacement field quite well, with variance reduction of more than 96%. Most of the misfit is concentrated near the

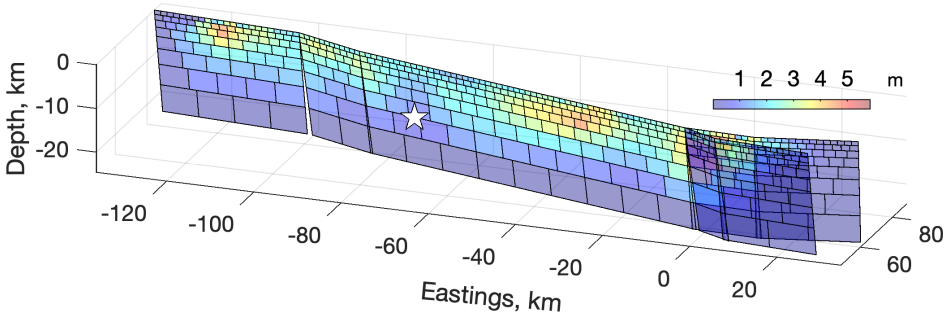

Figure 3. The preferred finite fault model obtained from inversions of Sentinel-1 SAR data (Figures 2 and S6), assuming a layered elastic half-space (Figure S4). White star denotes the earthquake hypocenter.

rupture trace, likely due to local undulations of the rupture trace, and/or off-fault yielding (e.g., Kaneko & Fialko, 2011). Figure 3 shows the best-fit model assuming the layered elastic half-space, and Figure S7 shows the respective model assuming the homogeneous elastic half-space. The main difference between the two sets of models is that the coseismic slip is somewhat shallower and on average smaller in case of a homogeneous half-space compared to a layered half-space, as expected (e.g., Fialko, 2004b).

We evaluate the geodetic moment magnitude $M_g = 2/3(\log_{10} GP - 9.1)$, where $G = 33$ GPa is the nominal shear modulus, and P is the seismic potency, computed as an algebraic sum $\Sigma_{i=1}^{N} A_i S_i$, where N is the number of slip patches (dislocations), and A_i and S_i are the area of, and the amplitude of slip on, patch i. The respective values of M_g are 7.43 and 7.46 for the homogeneous and layered models, respectively. We also computed an equivalent moment tensor for the best-fit slip model (Figure 3) by computing a tensorial sum of moment tensors of all individual dislocations (e.g., Fialko, 2021). The respective focal mechanism is shown as a green beach ball in Figure 1, and is in a good agreement with the CMT solution (Ekström et al., 2012).

Discussion and conclusions

The moment magnitude obtained from inversions of the Sentinel-1 SAR data (M_g ~7.4; Figures 2-3) falls within the range of the moment magnitudes determined from seismic data based on the W-phase (M_w =7.3, USGS, 2021a) and the centroid moment tensor (M_w =7.5 from the USGS catalog, USGS (2021b); M_w =7.4 from the Global CMT catalog, Ekström et al. (2012)). Our results are closer to the magnitude determined using the centroid moment tensor; the magnitude determined using the W-phase appears to be an under-estimate. The geodetic moment magnitude estimate is also in a good agreement with that from the USGS finite fault model which indicates the moment magnitude of 7.4 (USGS, 2021d). However, the details of fault geometry and slip distribution are notably different. The slip distribution determined from fitting the teleseismic data suggests the largest moment release to the west of the epicenter (USGS, 2021d). In contrast, our finite fault model reveals that the largest slip areas are located to the east of the epicenter (Figure 3). A larger moment release in the eastern part of the earthquake rupture is directly evident from the surface displacement data (e.g., Figure S3).

The USGS finite fault model also features a southward dip of the earthquake rupture, with a dip angle of 76 degrees (USGS, 2021d). Our best-fit model (Figure 3)

indicates that the fault that produced the 2021 Maduo earthquake dips to the north at ∼80 degrees. The misfit function does not preclude a vertical fault, but the southward dip appears unlikely (Figure S5). Observations that favor a non-vertical dip include larger displacements on the northern side of the fault (Figure S3). For a quasi-planar fault, such an asymmetry implies a fault dip to the north (e.g., Fialko, 2004b). A steep northward dip of a large part of the Maduo rupture was also inferred by Zhao et al. (2021) based on inversions of Sentinel-1 SAR data. Another possibility is a rigidity contrast between blocks separated by the earthquake rupture, with lower elastic moduli on the north side (e.g., Rybicki & Kasahara, 1977; Fialko, 2006). Initial studies of precisely located aftershocks appear to support the former interpretation (Wang et al., 2021; Zhao et al., 2021).

Bifurcation of slip observed at the eastern end of the earthquake rupture (Figure S3) appears to be a common feature of a number of major continental strike-slip earthquakes. Other documented cases of bifurcating ruptures include e.g. the 1992 M7.3 Landers (Sowers et al., 1994), 1999 M7.1 Hector Mine (Fialko et al., 2001), 2001 M7.8 Kokoxilli (Klinger et al., 2005), 2002 M7.9 Denali (Haeussler et al., 2004), 2015 M7.2 Sarez (Jin et al., 2021), and 2019 M7.1 Ridgecrest (Jin & Fialko, 2020) earthquakes. The observed fault branching may be an efficient mechanism for terminating dynamic ruptures, as slip on closely spaced sub-parallel fault strands acts to dissipate seismic energy and discourage slip on the adjacent strands.

The near-field displacements show variations in the degree of slip localization along the rupture trace (Figure S3). Such variations may indicate either distributed failure, or excess slip at depth (Fialko et al., 2005; Lindsey et al., 2014). Indeed, finite fault models representing earthquake rupture as dislocations in an elastic half-space show maximum slip in the middle of the seismogenic layer (Figures 3 and S8). This is similar to slip patterns of a number of M7+ earthquakes worldwide. Figure 4 shows a normalized distribution of slip as a function of depth for the M7.4 Maduo earthquake (black solid line) obtained from our best-fitting model for a layered half-space (Figure 3), as well as for several other strike-slip earthquakes of a comparable size (color dashed lines). The inferred 1-D slip distribution is not strongly affected by the model assumptions (layered vs. homogeneous half-space, Figure S8). As one can see from Figure 4, the maximum average slip due to the Maduo earthquake occurred in the depth interval between 3-4 km, similar to results obtained for other earthquakes, and also to the depth distribution of seismicity in California (Jin & Fialko, 2020). A more sharply peaked slip distribution of the 2019 Ridgecrest (California) earthquake may result from a geometric complexity (in particular, shallow splay faults, Jin & Fialko, 2020), but otherwise the slip patterns of most of the events appear remarkably consistent. The apparent shallow slip deficit (SSD) due to the Maduo earthquake is of the order of 30% (Figure 4).

Factors that can give rise to a reduced magnitude of coseismic slip at the Earth's surface inferred from kinematic inversions include velocity-strengthening properties of the uppermost crust (Marone & Scholz, 1988), reductions in elastic rigidity within a finite zone adjacent to a fault (Barbot, Fialko, & Sandwell, 2008), and dynamic off-fault damage (Fialko et al., 2005; Kaneko & Fialko, 2011). It was also argued that the amount of the SSD may inversely correlate with the earthquake magnitude and fault maturity (given that more mature faults are able to host larger earthquakes) (Dolan & Haravitch, 2014; Jin & Fialko, 2020). Sorting out between different factors is important for understanding the earthquake slip budget and partitioning of deformation throughout the seismic cycle.

In case of the velocity-strengthening behavior of the shallow Earth's crust, coseismic slip at the surface is expected to be suppressed compared to slip at greater depth, but there is no permanent SSD in that the coseismic slip deficit is taken up by aseismic creep that occurs between the earthquakes (e.g., Kaneko et al., 2013; Lind-

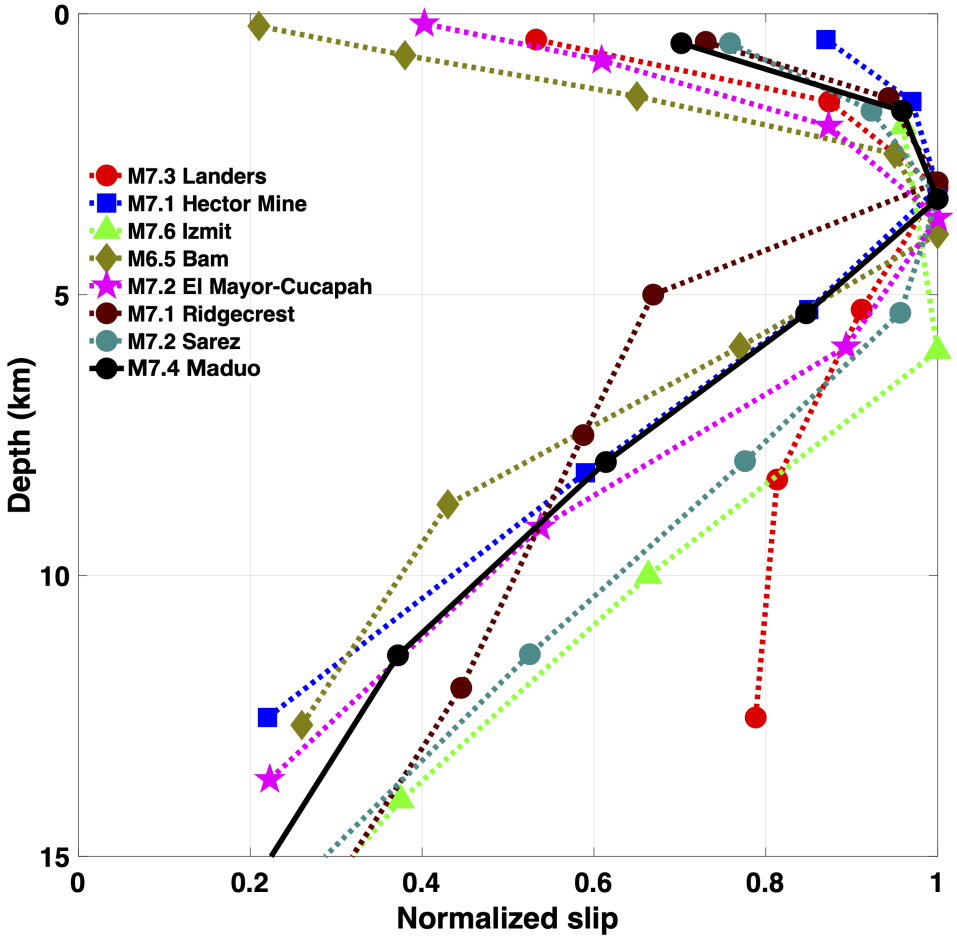

Figure 4. Along-strike averaged normalized coseismic slip as a function of depth for the 2021 M7.4 Maduo earthquake (black solid line), as well as for several other M∼7 strike-slip earthquakes (color dashed lines, data from Fialko et al. (2005); Jin and Fialko (2020)).

sey & Fialko, 2016). The presence of a velocity-strengthening layer is therefore most directly manifested in a shallow interseismic creep and postseismic afterslip (e.g., Barbot, Fialko, & Bock, 2009; LaBonte et al., 2009; Wei et al., 2015). To check if there is shallow afterslip following the 2021 Maduo earthquake, we generated postseismic interferograms acquired in the first month following the mainshock. All postseismic interferograms were unwrapped using SNAPHU (Chen & Zebker, 2000). Figure 5 shows the LOS displacements from different view directions corresponding to the ascending and descending satellite orbits. The postseismic interferograms reveal a displacement discontinuity following the rupture trace of the Maduo earthquake. The sense of motion agrees with the coseismic displacements (Figures 2 and S3), and the amplitude is of the order of tens of millimeters in the satellite line of sight (Figures 5 and S9), equivalent to ~ 0.1m of strike-slip. The early postseismic deformation measured with Sentinel-1 interferometry is therefore indicative of afterslip reaching to the Earth's surface, suggesting that at least part of the shallow coseismic slip deficit inferred for the Maduo earthquake (Figures 3 and 4) is due to the velocity-strengthening conditions above the seismogenic layer. We note that the largest amplitudes of shallow afterslip are observed in the central part of the earthquake rupture that on average produced smaller coseismic offsets (cf. Figures S3, 5, and S9), consistent with our interpretation.

Given that the available SAR data miss the first several days of postseismic deformation during which the afterslip rates are supposed to be the highest, and that the afterslip following large events can last years and decades (e.g., Barbot, Fialko, & Bock, 2009; Wang & Fialko, 2014, 2018; Özarpacı et al., 2021), it's conceivable that the total amount of afterslip may be substantially larger than that observed during the first month following the mainshock (Figures 5 and S9). In addition, a region that hosts afterslip can produce some amount of creep in the interseismic period, including a non-steady creep (e.g., Tymofyeyeva et al., 2019). This suggests that the Maduo earthquake does not present a compelling case for a long-term SSD, in contrast to other M7+ events for which the amount of shallow creep was deemed negligible or insufficient to make up for the inferred coseismic deficit (Figure 4). Additional observations combined with numerical modeling are needed to see if the amount of afterslip and interseismic creep on the Maduo fault cumulatively can be large enough to balance $\sim$0.5-1 m of slip in the top several kilometers of the Earth's crust (Figure S8).

It's worth noting that the wavelength of left-lateral postseismic displacements that produce a discontinuity across the fault trace (see Figures 5 and S9) is much larger than that expected of shallow afterslip. This may be due to the combined contributions of afterslip above and below the seismogenic zone, and possibly a robust aftershock activity (Figure 1; Barbot, Hamiel, & Fialko, 2008). A poro-elastic relaxation may also generate the near-field fault-parallel displacements having the same sense as the coseismic displacements (Fialko, 2004a). However, the dominant poro-elastic signal in the satellite line of sight should be associated with vertical displacements in regions of relative compression and extension near the rupture tips; such a signal is not clearly present in the data (Figure 5).

Continued space geodetic observations of the rupture area of the 2021 Maduo earthquake will provide valuable insights into the mechanical properties of the Earth's crust in Tibet, including the deeper rheologic structure and the associated time-dependent relaxation processes.

Acknowledgments
We thank two anonymous reviewers for comments that improved this manuscript. This study was supported by NSF (grant EAR-1841273) and NASA (grant 80NSSC18K0466). Figures were produced using Generic Mapping Tools (GMT) (Wessel et al., 2013) and Matlab.

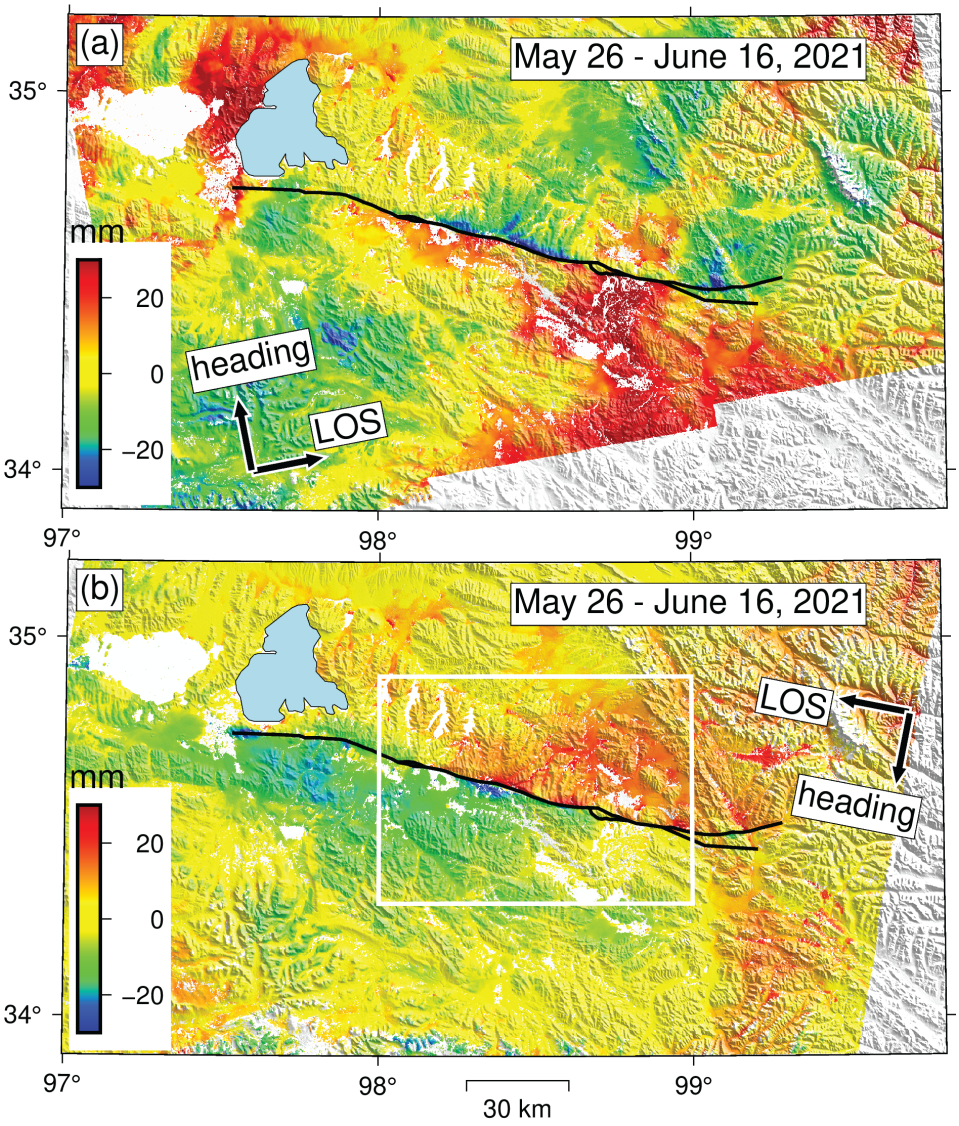

Figure 5. Postseismic interferograms spanning ∼1 month after the 2021 M7.4 Maduo earthquake from the ascending (a) and descending (b) Sentinel-1 tracks. The color scale is in millimeters. Positive LOS displacements are away from the satellite. White box outlines a close-up area shown in Figure S9.

Data Availability Statement

All data used is this study are open access. Primary data are available from the European Space Agency (ESA, `https://scihub.copernicus.eu`), with copies hosted at UNAVCO,
`https://winsar.unavco.org`, and Alaska SAR Facility (ASF,
`https://asf.alaska.edu/how-to/data-tools`). Data providers require user registration to gain access. List of granule names is provided in Table S1 in the Supporting Information.

Sub-sampled LOS displacements and range offsets used in this study are available at: DOI:10.5281/zenodo.5528331

Inversion codes used to generate results presented in this study are available at: DOI:10.5281/zenodo.5528639

References

Barbot, S., Fialko, Y., & Bock, Y. (2009). Postseismic deformation due to the Mw 6.0 2004 Parkfield earthquake: Stress-driven creep on a fault with spatially variable rate-and-state friction parameters. *J. Geophys. Res.*, *114*, B07405.

Barbot, S., Fialko, Y., & Sandwell, D. (2008). Effect of a compliant fault zone on the inferred earthquake slip distribution. *J. Geophys. Res.*, *113*, B06404, doi:10.1029/2007JB005256.

Barbot, S., Fialko, Y., & Sandwell, D. (2009). Three-dimensional models of elastostatic deformation in heterogeneous media, with applications to the Eastern California Shear Zone. *Geophys. J. Int.*, *179*, 500–520.

Barbot, S., Hamiel, Y., & Fialko, Y. (2008). Space geodetic investigation of the co- and post-seismic deformation due to the 2003 M_w 7.1 Altai earthquake: Implications for the local lithospheric rheology. *J. Geophys. Res.*, *113*, B03403.

Chen, C. W., & Zebker, H. A. (2000). Network approaches to two-dimensional phase unwrapping: intractability and two new algorithms. *J. Opt. Soc. Am. A*, *17*(3), 401–414. doi: 10.1364/JOSAA.17.000401

Dolan, J. F., & Haravitch, B. D. (2014). How well do surface slip measurements track slip at depth in large strike-slip earthquakes? the importance of fault structural maturity in controlling on-fault slip versus off-fault surface deformation. *Earth Planet. Sci. Lett.*, *388*, 38–47.

Dutta, R., Jónsson, S., & Vasyura-Bathke, H. (2021). Simultaneous Bayesian estimation of non-planar fault geometry and spatially-variable slip. *J. Geophys. Res.*, e2020JB020441.

Ekström, G., Nettles, M., & Dziewoński, A. (2012). The global CMT project 2004–2010: Centroid-moment tensors for 13,017 earthquakes. *Physics of the Earth and Planetary Interiors*, *200*, 1–9.

Farr, T., & Kobrick, M. (2000). Shuttle Radar Topography Mission produces a wealth of data. *AGU Eos*, *81*, 583–585.

Fialko, Y. (2004a). Evidence of fluid-filled upper crust from observations of post-seismic deformation due to the 1992 M_w7.3 Landers earthquake. *J. Geophys. Res.*, *109*, B08401, 10.1029/2004JB002985.

Fialko, Y. (2004b). Probing the mechanical properties of seismically active crust with space geodesy: Study of the co-seismic deformation due to the 1992 M_w7.3 Landers (southern California) earthquake. *J. Geophys. Res.*, *109*, B03307, 10.1029/2003JB002756.

Fialko, Y. (2006). Interseismic strain accumulation and the earthquake potential on the southern San Andreas fault system. *Nature*, *441*, 968–971.

Fialko, Y. (2021). Estimation of absolute stress in the hypocentral region of the 2019 Ridgecrest, California, earthquakes. *J. Geophys. Res.*, *126*, e2021JB022000.

Fialko, Y., Sandwell, D., Simons, M., & Rosen, P. (2005). Three-dimensional deformation caused by the Bam, Iran, earthquake and the origin of shallow slip deficit. *Nature*, *435*, 295–299.

Fialko, Y., Simons, M., & Agnew, D. (2001). The complete (3-D) surface displacement field in the epicentral area of the 1999 M_w7.1 Hector Mine earthquake, southern California, from space geodetic observations. *Geophys. Res. Lett.*, *28*, 3063–3066.

Funning, G. J., Parsons, B., & Wright, T. J. (2007). Fault slip in the 1997 Manyi, Tibet earthquake from linear elastic modelling of InSAR displacements. *Geophys. J. Int.*, *169*, 988–1008.

Goldstein, R. M., Zebker, H. A., & Werner, C. L. (1988). Satellite radar interferometry: Two-dimensional phase unwrapping. *Radio science*, *23*(4), 713–720.

Golub, G. H., Hansen, P. C., & O'Leary, D. P. (1999). Tikhonov regularization and total least squares. *SIAM journal on matrix analysis and applications*, *21*(1), 185–194.

Guo, J., Lin, A., Sun, G., & Zheng, J. (2007). Surface ruptures associated with the 1937 M7.5 Tuosuo Lake and the 1963 M7.0 Alake Lake earthquakes and the paleoseismicity along the Tuosuo Lake segment of the Kunlun fault, northern Tibet. *Bull. Seism. Soc. Am.*, *97*, 474–496.

Haeussler, P. J., Schwartz, D. P., Dawson, T. E., Stenner, H. D., Lienkaemper, J. J., Sherrod, B., ... others (2004). Surface rupture and slip distribution of the Denali and Totschunda faults in the 3 November 2002 M 7.9 earthquake, Alaska. *Bull. Seism. Soc. Am.*, *94*, S23–S52.

Jin, Z., & Fialko, Y. (2020). Finite slip models of the 2019 Ridgecrest earthquake sequence constrained by space geodetic data and aftershock locations. *Bull. Seism. Soc. Am.*, *110*, 1660–1679. doi: 10.1785/0120200060

Jin, Z., Fialko, Y., Zubovich, A., & Schöne, T. (2021). Lithospheric deformation due to the 2015 M7.2 Sarez (Pamir) earthquake constrained by 5 years of space geodetic observations. *preprint*. doi: 10.1002/essoar.10508106.1

Jonsson, S., Zebker, H., Segall, P., & Amelung, F. (2002). Fault slip distribution of the 1999 M_w 7.1 Hector Mine, California, earthquake, estimated from satellite radar and GPS measurements. *Bull. Seism. Soc. Am.*, *92*, 1377–1389.

Kaneko, Y., & Fialko, Y. (2011). Shallow slip deficit due to large strike-slip earthquakes in dynamic rupture simulations with elasto-plastic off-fault response. *Geophys. J. Int.*, *186*, 1389–1403.

Kaneko, Y., Fialko, Y., Sandwell, D., Tong, X., & Furuya, M. (2013). Interseismic deformation and creep along the central section of the North Anatolian Fault (Turkey): InSAR observations and implications for rate-and-state friction properties. *J. Geophys. Res.*, *118*(1), 316–331.

Klinger, Y., Xu, X., Tapponnier, P., Van der Woerd, J., Lasserre, C., & King, G. (2005). High-resolution satellite imagery mapping of the surface rupture and slip distribution of the Mw7.8, 14 November 2001 Kokoxili earthquake, Kunlun fault, northern Tibet, China. *Bull. Seism. Soc. Am.*, *95*, 1970–1987.

LaBonte, A., Brown, K., & Fialko, Y. (2009). Hydrogeologic detection and finite-element modeling of a slow-slip event in the Costa Rica prism toe. *J. Geophys. Res.*, *114*, B00A02. doi: 10.1029/2008JB005806

Lin, G., Shearer, P. M., & Fialko, Y. (2006). Obtaining absolute locations for quarry seismicity using remote sensing data. *Bull. Seism. Soc. Am.*, *96*, 722-728.

Lindsey, E. O., & Fialko, Y. (2016). Geodetic constraints on frictional properties and earthquake hazard in the Imperial Valley, Southern California. *J. Geophys. Res.*, *121*, 1097–1113.

Lindsey, E. O., Fialko, Y., Bock, Y., Sandwell, D. T., & Bilham, R. (2014). Localized and distributed creep along the southern San Andreas Fault. *J. Geophys. Res.*, *119*(10), 7909–7922.

Marone, C., & Scholz, C. H. (1988). The depth of seismic faulting and the upper

transition from stable to unstable slip regimes. *Geophys. Res. Lett.*, *15*, 621–624.

Okada, Y. (1985). Surface deformations due to shear and tensile faults in a halfspace. *Bull. Seism. Soc. Am.*, *75*, 1135–1154.

Özarpacı, S., Doğan, U., Ergintav, S., Çakır, Z., Özdemir, A., Floyd, M., & Reilinger, R. (2021). Present GPS velocity field along 1999 Izmit rupture zone: evidence for continuing afterslip 20 yr after the earthquake. *Geophys. J. Int.*, *224*, 2016–2027.

Rybicki, K., & Kasahara, K. (1977). A strike-slip fault in a laterally inhomogeneous medium. *Tectonophysics*, *42*, 127–138.

Sandwell, D., Mellors, R., Tong, X., Wei, M., & Wessel, P. (2011). Open radar interferometry software for mapping surface deformation. *Eos, Trans. AGU*, *92*(28), 234–234.

Searle, M. P., Elliott, J., Phillips, R., & Chung, S.-L. (2011). Crustal–lithospheric structure and continental extrusion of Tibet. *Journal of the Geological Society*, *168*, 633–672.

Simons, M., Fialko, Y., & Rivera, L. (2002). Coseismic deformation from the 1999 M_w7.1 Hector Mine, California, earthquake, as inferred from InSAR and GPS observations. *Bull. Seism. Soc. Am.*, *92*, 1390–1402.

Sowers, J., Unruh, J., Lettis, W., & Rubin, T. (1994). Relationship of the Kickapoo fault to the Johnson Valley and Homestead Valley faults, San Bernardino County, California. *Bull. Seism. Soc. Am.*, *84*, 528–536.

Tapponnier, P., Peltzer, G., Le Dain, A., Armijo, R., & Cobbold, P. (1982). Propagating extrusion tectonics in Asia: New insights from simple experiments with plasticine. *Geology*, *10*(12), 611–616.

Taylor, M., & Yin, A. (2009). Active structures of the Himalayan-Tibetan orogen and their relationships to earthquake distribution, contemporary strain field, and Cenozoic volcanism. *Geosphere*, *5*, 199–214.

Thatcher, W. (2007). Microplate model for the present-day deformation of tibet. *J. Geophys. Res.*, *112*, B01401.

Tymofyeyeva, E., & Fialko, Y. (2015). Mitigation of atmospheric phase delays in InSAR data, with application to the Eastern California Shear Zone. *J. Geophys. Res.*, *120*, 5952–5963.

Tymofyeyeva, E., Fialko, Y., Jiang, J., Xu, X., Sandwell, D., Bilham, R., ... Moafipoor, S. (2019). Slow slip event on the southern San Andreas fault triggered by the 2017 M_w8.2 Chiapas (Mexico) earthquake. *J. Geophys. Res.*, *124*, 9956–9975.

USGS. (2021a). Retrieved from `https://earthquake.usgs.gov/earthquakes/eventpage/us7000e54r/moment-tensor?source=us&code=us_7000e54r_mww` (last accessed Jun 2021)

USGS. (2021b). Retrieved from `https://earthquake.usgs.gov/earthquakes/eventpage/us7000e54r/moment-tensor?source=us&code=us_7000e54r_mwc` (last accessed Jun 2021)

USGS. (2021c). Retrieved from `https://earthquake.usgs.gov/earthquakes/eventpage/iscgem902908` (last accessed Jun 2021)

USGS. (2021d). Retrieved from `https://earthquake.usgs.gov/earthquakes/eventpage/us7000e54r/finite-fault` (last accessed Jun 2021)

Wang, K., & Fialko, Y. (2014). Space geodetic observations and models of postseismic deformation due to the 2005 M7.6 Kashmir (Pakistan) earthquake. *J. Geophys. Res.*, *119*(9), 7306–7318.

Wang, K., & Fialko, Y. (2015). Slip model of the 2015 M_w 7.8 Gorkha (Nepal) earthquake from inversions of ALOS-2 and GPS data. *Geophys. Res. Lett.*, *42*, 7452–7458. doi: 10.1002/2015GL065201

Wang, K., & Fialko, Y. (2018). Observations and modeling of co- and postseismic deformation due to the 2015 M_w 7.8 Gorkha (Nepal) earthquake. *J. Geophys.*

Res., *123*(1), 761–779.

Wang, K., Xu, X., & Fialko, Y. (2017). Improving burst alignment in TOPS interferometry with bivariate enhanced spectral diversity (BESD). *IEEE Geoscience and Remote Sensing Letters*, *14*, 2423–2427.

Wang, R., Martin, F., & Roth, F. (2003). Computation of deformation induced by earthquakes in a multi-layered elastic crust - FORTRAN programs EDGRN/EDCMP. *Comp. Geosci.*, *29*, 195–207.

Wang, W., Fang, L., Wu, J., Tu, H., Chen, L., Lai, G., & Zhang, L. (2021). Aftershock sequence relocation of the 2021 Ms7.4 Maduo Earthquake, Qinghai, China. *Science China Earth Sciences*, 1–10.

Wei, S., Barbot, S., Graves, R., Lienkaemper, J. J., Wang, T., Hudnut, K., ... Helmberger, D. (2015). The 2014 Mw 6.1 South Napa earthquake: A unilateral rupture with shallow asperity and rapid afterslip. *Seismol. Res. Lett.*, *86*, 344–354.

Wessel, P., Smith, W. H. F., Scharroo, R., Luis, J., & Wobbe, F. (2013). Generic Mapping Tools: Improved Version Released. *Eos, Trans. AGU*, *94*, 409–410.

Zhao, D., Qu, C., Chen, H., Shan, X., Song, X., & Gong, W. (2021). Tectonic and geometric control on fault kinematics of the 2021 Mw7.3 Maduo (China) earthquake inferred from interseismic, coseismic and postseismic InSAR observations. *Geophys. Res. Lett.*, e2021GL095417.

Supporting Information for "Coseismic and early postseismic deformation due to the 2021 M7.4 Maduo (China) earthquake"

Zeyu Jin[1], Yuri Fialko[1]

[1]Institute of Geophysics and Planetary Physics, Scripps Institution of Oceanography, University of California, San Diego, La Jolla, California, USA.

Contents of this file

Tables S1 and S2

Figures S1 to S9

Table S1: SAR scenes used in this study. Spatial coverage of the combined scenes is shown in Figure 1 in the main text.

Satellite heading and track number	Granule name
Ascending 99	S1A_IW_SLC__1SDV_20210520T112611_20210520T112638_037971_047B4F
Ascending 99	S1A_IW_SLC__1SDV_20210520T112636_20210520T112704_037971_047B4F
Ascending 99	S1B_IW_SLC__1SDV_20210526T112525_20210526T112555_027075_033C0F
Ascending 99	S1B_IW_SLC__1SDV_20210526T112553_20210526T112628_027075_033C0F
Descending 106	S1A_IW_SLC__1SDV_20210520T232755_20210520T232822_037978_047B84
Descending 106	S1A_IW_SLC__1SDV_20210520T232820_20210520T232847_037978_047B84
Descending 106	S1B_IW_SLC__1SDV_20210526T232726_20210526T232756_027082_033C48
Descending 106	S1B_IW_SLC__1SDV_20210526T232754_20210526T232829_027082_033C48

Table S2: Interferometric pairs used in this study.

Satellite orbit and track number	Interferometric pairs	Time span (days)	Satellites	$B_\perp$ (m)[1]
Ascending 99	2021/05/20–2021/05/26	6	Sentinel-1A/B	51
Descending 106	2021/05/20–2021/05/26	6	Sentinel-1A/B	119

[1] Perpendicular baseline. Smaller perpendicular baselines ($B_\perp$) result in a better correlation of the radar phase.

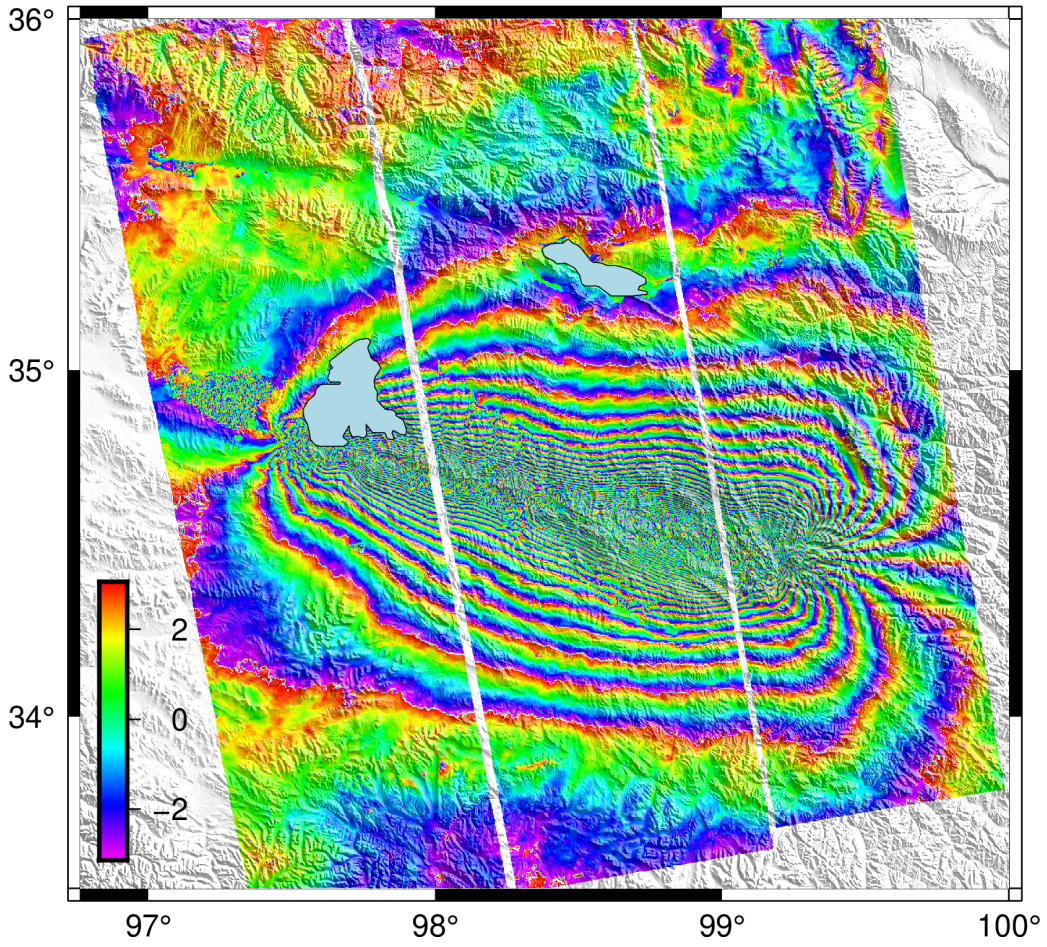

Figure S1: Coseismic interferogram of the 2021 Maduo earthquake from the Sentinel-1 ascending track 99. Color scale is in radians. Data were acquired on May 20 and 26, 2021. Each fringe corresponds to surface displacements of 28 mm in the satellite line of sight (LOS). Positive range changes indicate motion away from the satellite.

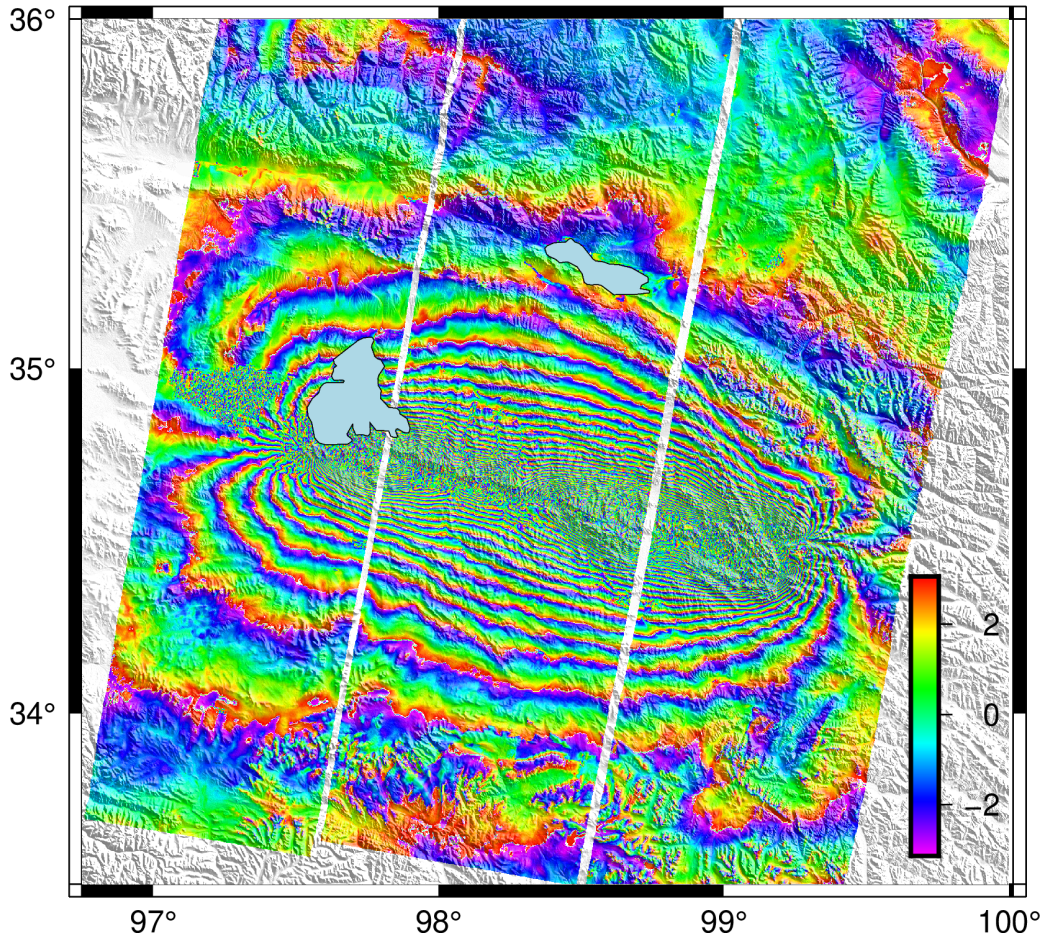

Figure S2: Coseismic interferogram of the 2021 Maduo earthquake from the Sentinel-1 descending track 106. Color scale is in radians. Data were acquired on May 20 and 26, 2021. Notation is the same as in Figure S1.

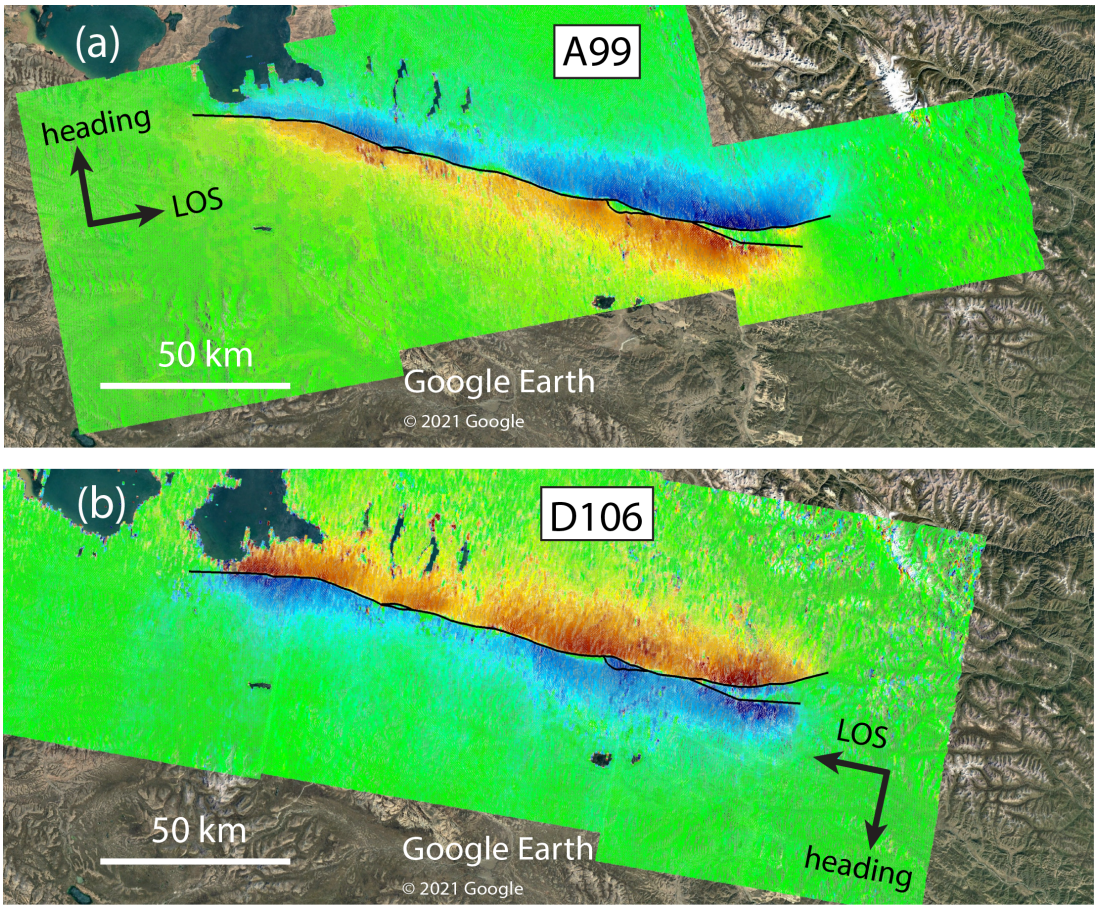

Figure S3: Range offsets from the ascending (a) and descending (b) Sentinel-1 tracks 99 and 106, respectively. Each panel has geographic bounds 97-100 deg. E, 34-35 deg. N. Color limits are the same as in Figure S6 (±1.5 m). Black wavy line denotes the fault trace determined from a joint interpretation of data shown in panels (a) and (b). The fault trace constrained by the coseismic pixel offsets was verified and refined using postseismic interferograms that revealed phase discontinuities due to shallow afterslip (Figure 5 in the main text).

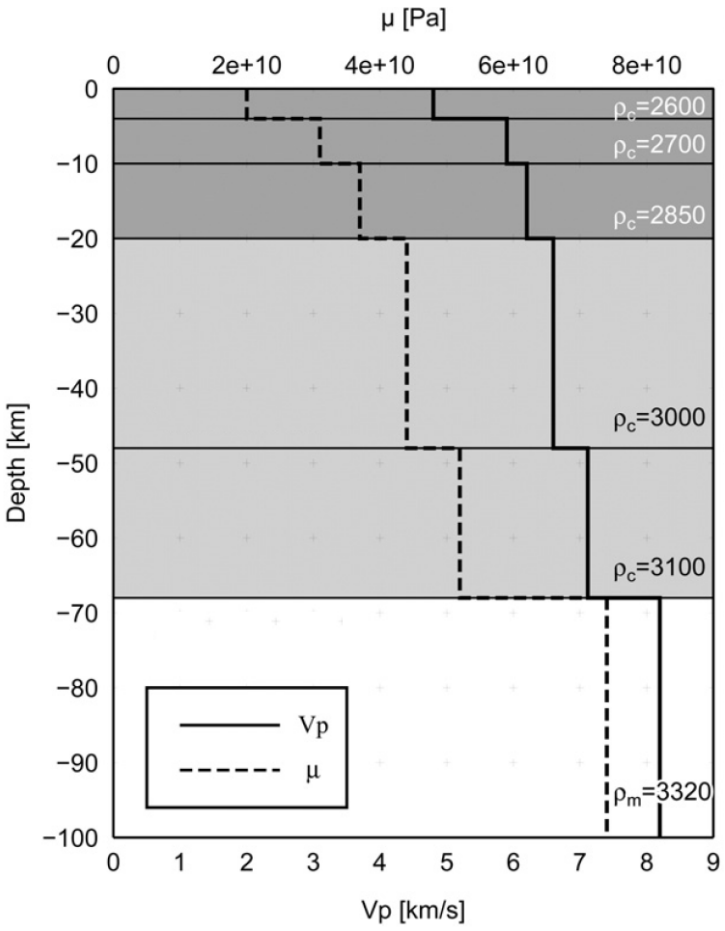

Figure S4: One-dimensional rigidity structure of the north-eastern Tibet used in our layered elastic half-space models. Top horizontal axis: shear modulus μ, bottom horizontal axis: P-wave velocity V_p. ρ_c and ρ_m are the densities of the Earth's crust and mantle, respectively, in kg/m^3. From Xiong, Shan, Zheng, and Wang (2010).

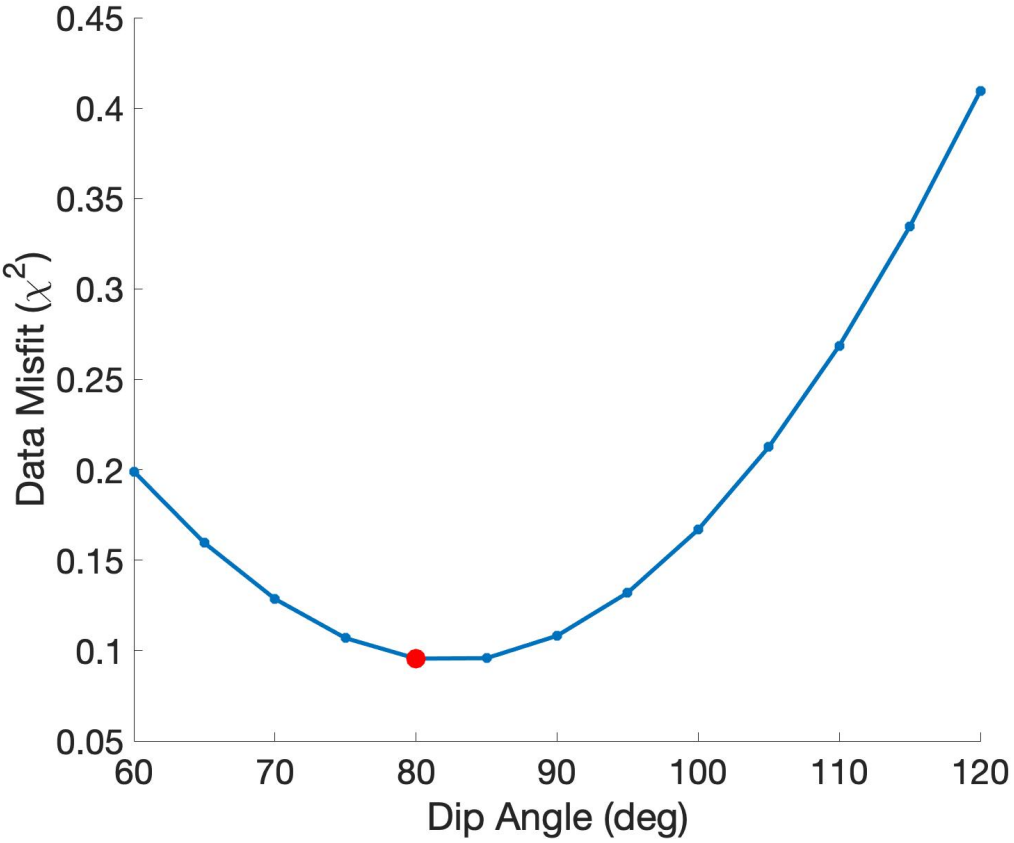

Figure S5: Model misfit as a function of the assumed fault dip angle.

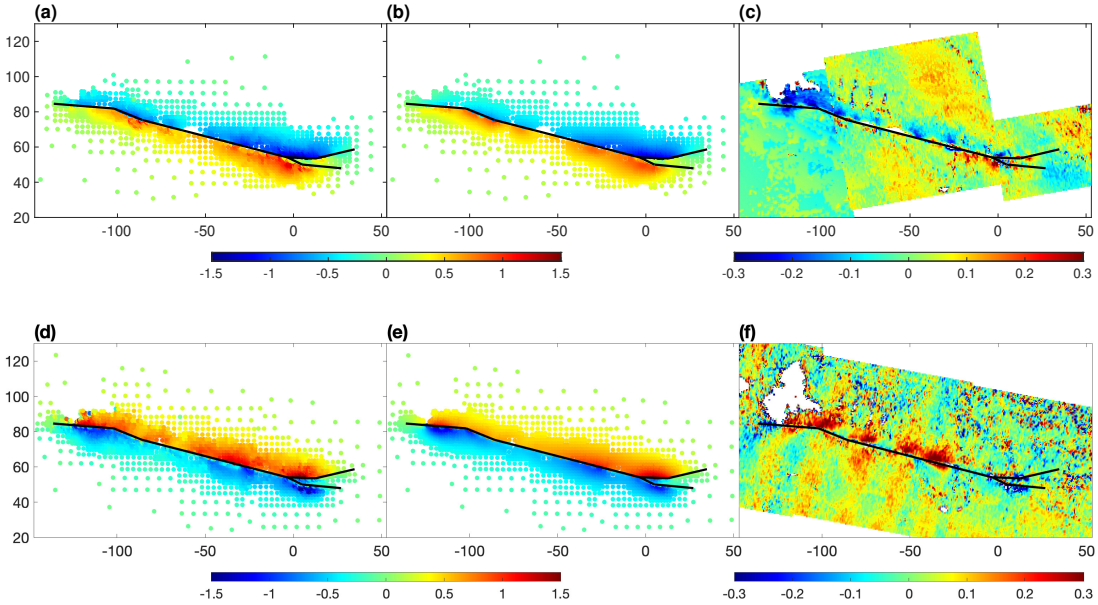

Figure S6: Sub-sampled coseismic range offsets (a,d), best-fit model predictions (b, e), and residuals (c, f) from the ascending (a-c) and descending (d-f) Sentinel-1 tracks (see Figures 1 and S3). Other notation is the same as in Figure 2 in the main text. Low-amplitude semi-periodic "stripes" apparent in the range offset residuals are artifacts, possibly due to ionospheric perturbations.

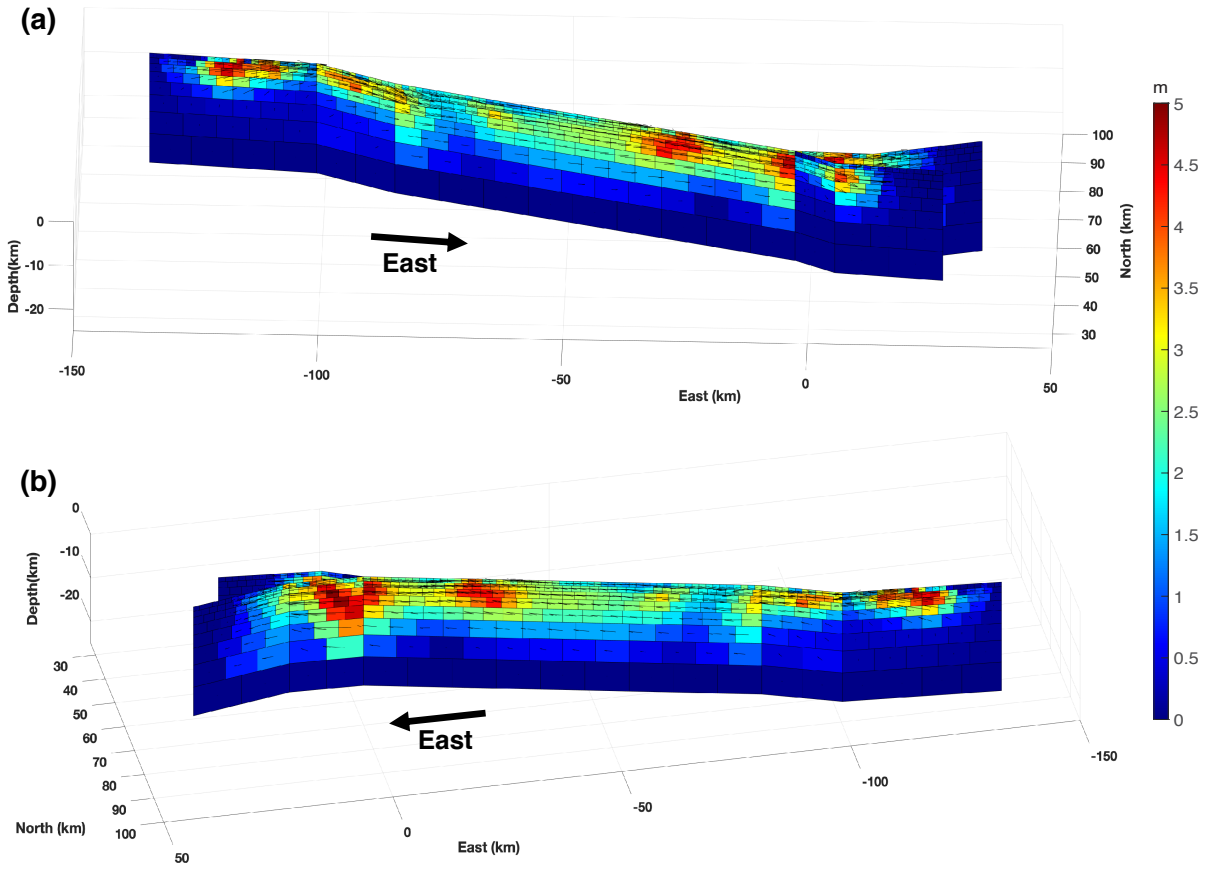

Figure S7: Fault slip model assuming a homogeneous layered elastic half-space (Okada, 1985). (a) view from the south; (b) view from the north. Color scale is in meters.

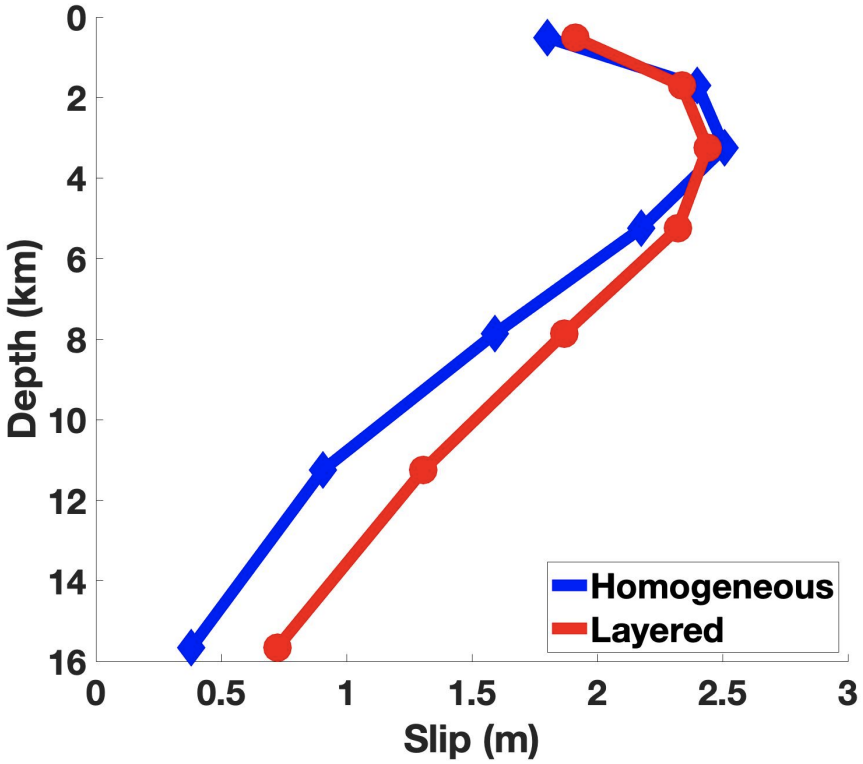

Figure S8: A comparison of the average coseismic slip as a function of depth obtained from inverse models assuming a homogeneous (blue line) and layered (red line) elastic half-space models.

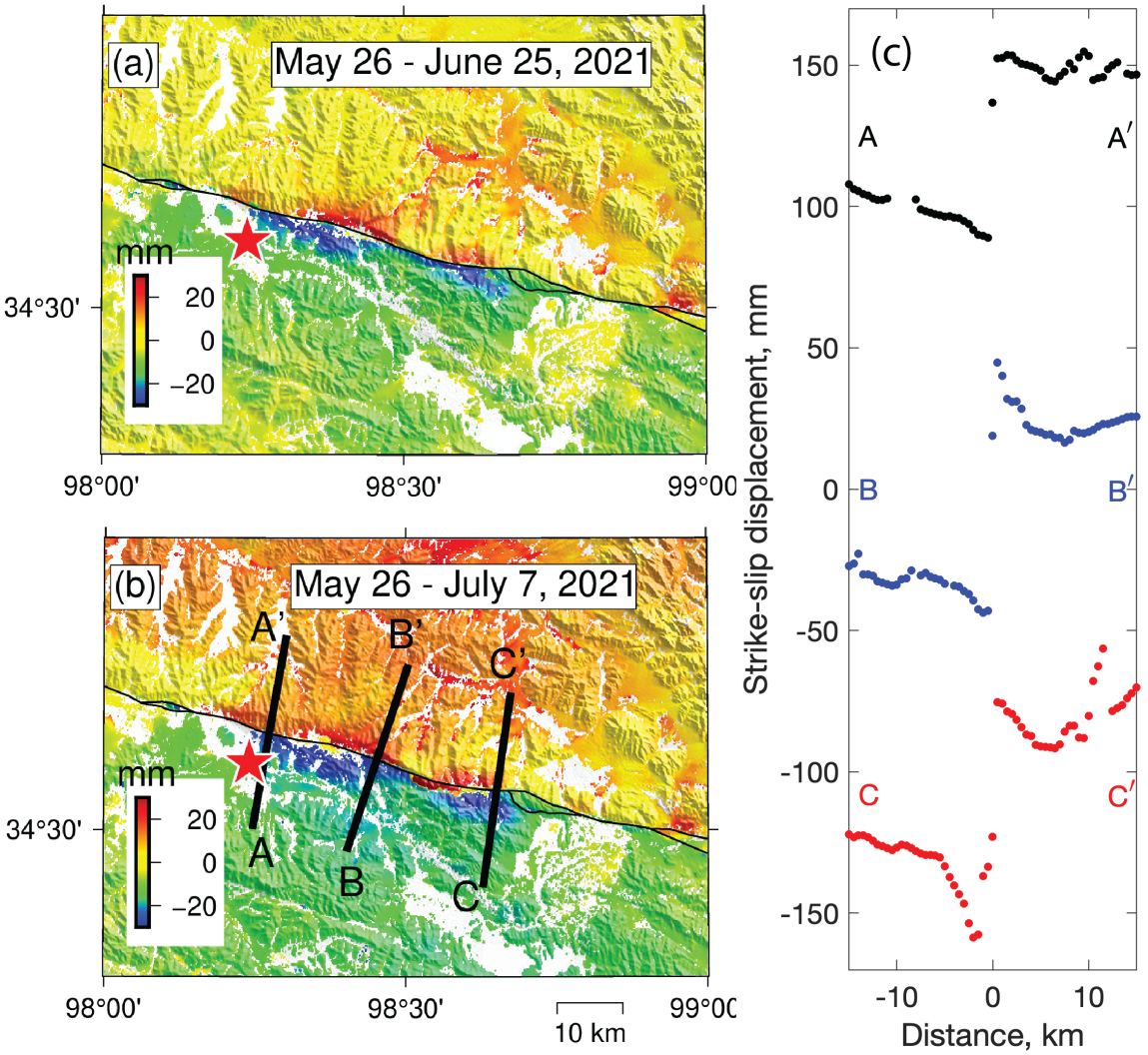

Figure S9: Enhanced shallow afterslip in the central part of the earthquake rupture that produced relatively small coseismic offsets (cf. Figure S3). Colors denote LOS displacements, in millimeters, from the descending Sentinel-1 track 106 (panels a, b). Black wavy line denotes the fault trace. Red star denotes the earthquake epicenter. In panel (b), thick black lines denote across-fault profiles shown in panel (c). In panel (c), LOS displacements have been converted to strike-slip displacements, assuming negligible vertical and fault-normal displacements (e.g., Fialko et al., 2002).

References

Fialko, Y., Sandwell, D., Agnew, D., Simons, M., Shearer, P., & Minster, B. (2002). Deformation on nearby faults induced by the 1999 Hector Mine earthquake. *Science*, *297*, 1858–1862.

Okada, Y. (1985). Surface deformation due to shear and tensile faults in a half-space. *Bull. Seismol. Soc. Am.*, *75*, 1135–1154.

Xiong, X., Shan, B., Zheng, Y., & Wang, R. (2010). Stress transfer and its implication for earthquake hazard on the Kunlun Fault, Tibet. *Tectonophysics*, *482*, 216–225.